Soil Dynamics and Earthquake Engineering 164 (2023) 107569

Contents lists available at ScienceDirect

Soil Dynamics and Earthquake Engineering

journal homepage: www.elsevier.com/locate/soildyn

# Two-dimensional simulation of the seismic response of the Santiago Basin, Chile

José Bustos [a], César Pastén [a,*], Diego Pavez [b], Miguel Acevedo [c], Sergio Ruiz [d], Rodrigo Astroza [e]

[a] Department of Civil Engineering, University of Chile, Chile
[b] Geotechnical Engineer, Wood, Chile
[c] Geotechnical Engineer, Itasca, Chile
[d] Department of Geophysics, University of Chile, Chile
[e] Facultad de Ingeniería y Ciencias Aplicadas, Universidad de los Andes, Chile

ARTICLE INFO

*Keywords:*
Site effects
Seismic amplification
Amplification factor
Aggravation factor
Numerical modelling
Shear-wave velocity model

ABSTRACT

Results from an ambient noise tomography, gravimetric studies, and local geophysical surveys are combined to develop three representative cross-sections of the Santiago Basin, Chile, that include the main geological features and the wave velocities of the materials. One-dimensional (1D) and two-dimensional (2D) seismic responses were simulated for each cross-section, considering input seismic signals polarized in different directions. Amplification factors calculated in the surface of the cross-sections highlight the larger amplitudes and durations of the strong-ground motions in the softer deposits of the Basin due to surface waves generated at the boundaries of the rock outcrops. 2D over 1D aggravation factors for several earthquake ground motion characteristics indicate that 2D effects are negligible in the stiff gravel deposits and that the 1D simulations cannot capture the basin edge effects in the fine-grained soils. Numerical predictions are confirmed using the analyses of earthquake records of the 2015 Mw 8.3 Illapel Earthquake.

## 1. Introduction

Central Chile is located in a highly active seismotectonic region controlled by the subduction of the oceanic Nazca plate underneath the continental South American plate, which causes large megathrust earthquakes with relatively high frequency [1]. The city of Santiago (Fig. 1) was founded on a sedimentary basin located in the central region of continental Chile. The Santiago Basin extends 90 km in the north-south direction and 40 km in the east-west direction. Araneda et al. [3], González et al. [4], and Yañez et al. [5] developed gravimetric studies along the Basin showing irregular morphology with relatively shallow quaternary deposits (average depth of 200 m) with three main depocenters reaching maximum depths of approximately 600 m. The main differences in the bedrock depth are due to the spatial distribution of the adopted datasets.

Several earthquakes have struck the Santiago Basin in the last decades (Fig. 1). The last megathrust earthquake was the 2015 Mw 8.3 Illapel Earthquake, which occurred at approximately 220 km north of the Santiago city [6,7]. No damage was reported and several seismological stations recorded this event in the Basin (e.g., stations R02M, R12M, R14M, R18M, R21M, and R22M shown in Fig. 1). The most destructive recent earthquakes were the 1985 Mw 8.0 Valparaiso and the 2010 Mw 8.8 Maule Earthquakes [1]. The structural damage during these events concentrated in the northwestern part of the Basin, area predominantly composed of fine-grained soils. This evidence indicates that surface geology has a strong influence on the seismic response of the Basin [2]. Proof of this amplification is that the seismic MSK-64 intensities over silty, clayey, and ignimbrite deposits were estimated at 7.5, while intensities over stiffer gravel deposits were lower than 6.0 [8,9]. The high intensities recorded in the northwestern fine-grained soils are directly related to the lower shear-wave velocities (Vs) and the larger depths of these deposits, which result in low predominant vibration frequencies. These amplification patterns were newly observed during the 2010 Mw 8.8 Maule Earthquake [2,10], confirming the influence of the surface geology on the seismic response of the Basin. The seismic response becomes even more relevant since a large megathrust earthquake is expected as a recurrent event of the 1730 Mw~9.0 Central Chile earthquake (Fig. 1, [1].

* Corresponding author. Av. Blanco Encalada 2002, Of. 431, Santiago, 8370449, Chile
*E-mail addresses:* jose.bustos.f@ug.uchile.cl (J. Bustos), cpasten@uchile.cl (C. Pastén), dpavezcarrillo@gmail.com (D. Pavez), miguelcvd91@gmail.com (M. Acevedo), sruiz@uchile.cl (S. Ruiz), rastroza@miuandes.cl (R. Astroza).

https://doi.org/10.1016/j.soildyn.2022.107569
Received 19 July 2022; Received in revised form 28 September 2022; Accepted 29 September 2022
Available online 12 October 2022

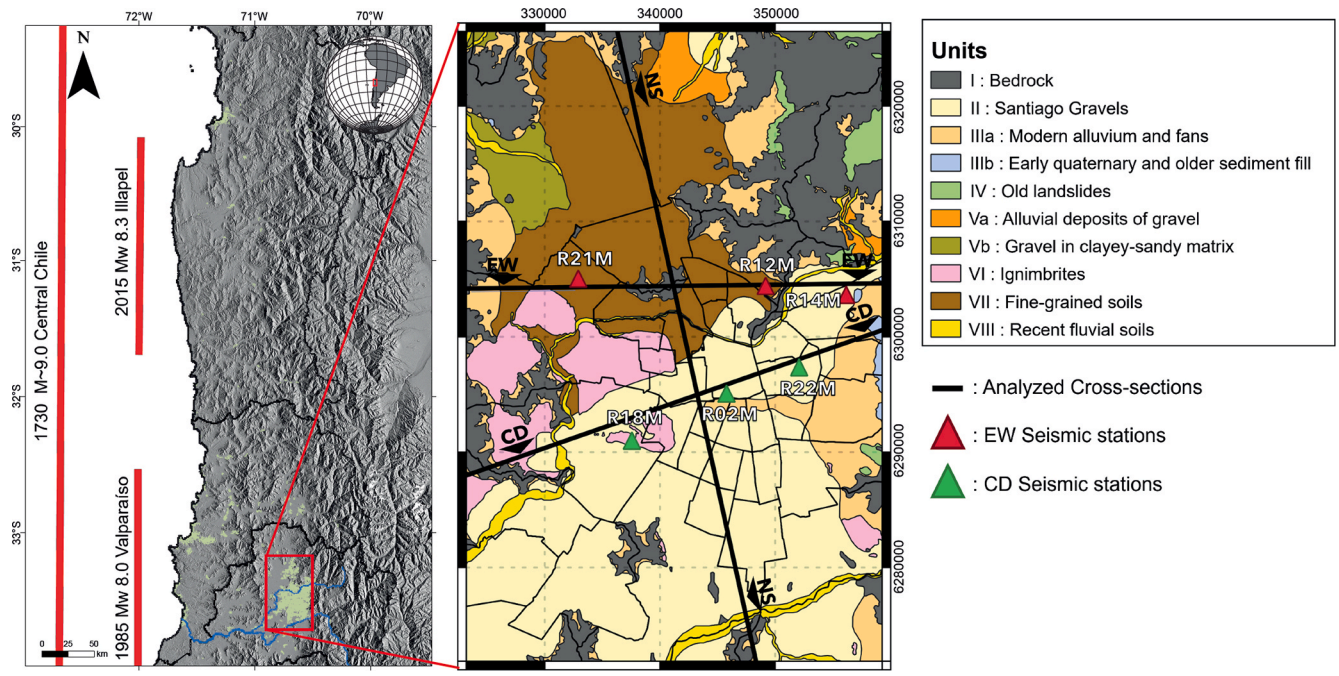


**Fig. 1.** Surface geology of the Santiago Basin proposed by Leyton et al. [2] and the cross-sections analyzed in this study. Triangles represent the location of the seismic stations that recorded the 2015 Mw 8.3 Illapel Earthquake.

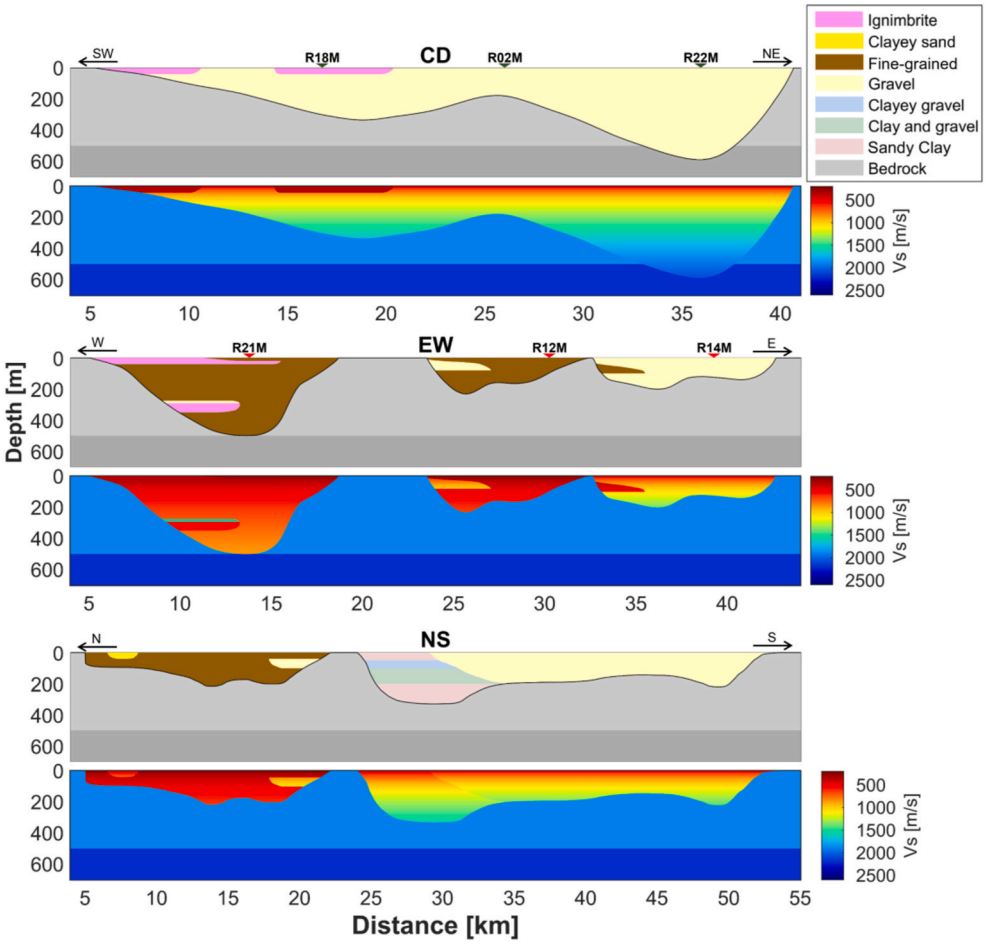


**Fig. 2.** CD, EW, and NS cross-sections with the geological information at the top panels and the Vs models at the bottom panels.

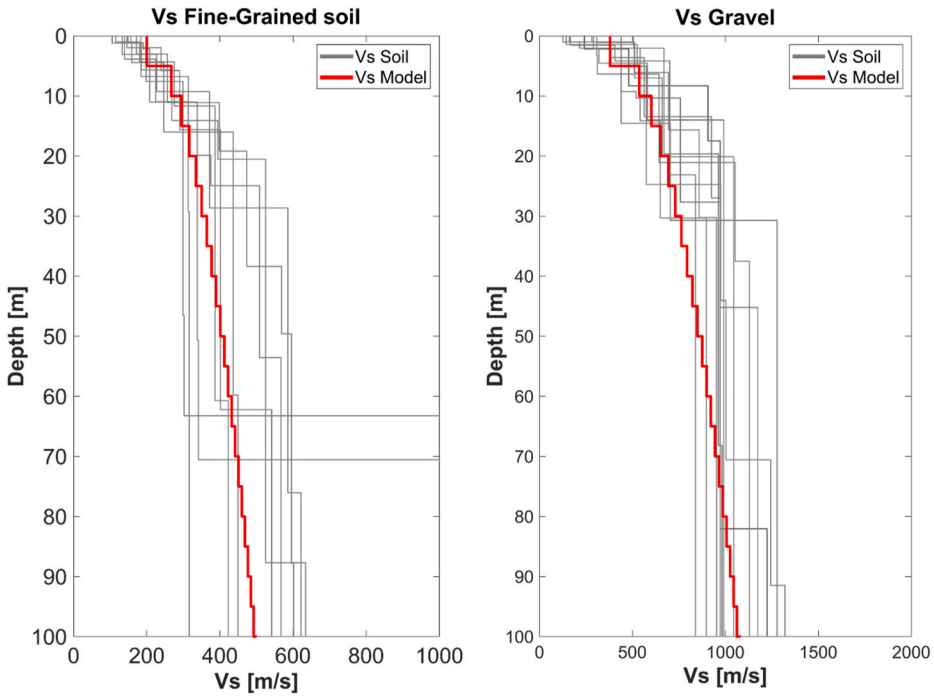


**Fig. 3.** Shear wave velocity (Vs) profiles of sites over Santiago gravels and fine-grained soils up to a depth of 100 m. The thick red lines are the simplified Vs models used in the cross-sections for simulations.

**Table 1**
Dynamic soil parameters.

| Soil type | $Vs_0$ (m/s) | dVs (m/s) | Density (kg/m$^3$) |
|---|---|---|---|
| Gravel | 380 | 70 | 2100 |
| Clayey sand | 300 | 70 | 2100 |
| Gravel and clay | 300 | 70 | 2000 |
| Sandy clay | 300 | 70 | 1900 |
| Clayey Gravel | 300 | 70 | 1900 |
| Fine-grained | 200 | 30 | 1600 |

The Santiago Basin has been addressed in several studies in order to identify and explain the factors that cause the observed seismic site effects. Bonnefoy-Claudet et al. [11] and Pastén [12] estimated predominant frequencies of the fine-grained deposits in the northern part of the Basin using the H/V spectral ratio method (HVSR [13,14], among others), finding that the frequencies vary inversely proportional to the depth of the sedimentary cover. These studies were unable to identify predominant frequencies in stiffer soils, such as gravels and alluvial soils, because the HVSRs tend to flat in the analyzed frequency range (0.2–20 Hz) with amplitudes lower than two. The large HVSR amplitudes on fine-grained soils indicate large impedance contrasts between the soils and the underlying bedrock, which may be related to large seismic amplification. In contrast, the lower HVSR amplitudes on stiffer soils are consistent with lower seismic amplifications observed during recent earthquakes. Pilz et al. [15] performed 3D numerical simulations of the Santiago Basin using a deterministic wave propagation tool based on the spectral element method, considering the soil as a single quaternary unit with the Vs model proposed by Pilz et al. [16], the surface topography from a digital elevation model, and the bedrock depth from the gravimetric studies mentioned above. The 3D simulations predict a significantly higher ground-motion level in the deep deposits of the

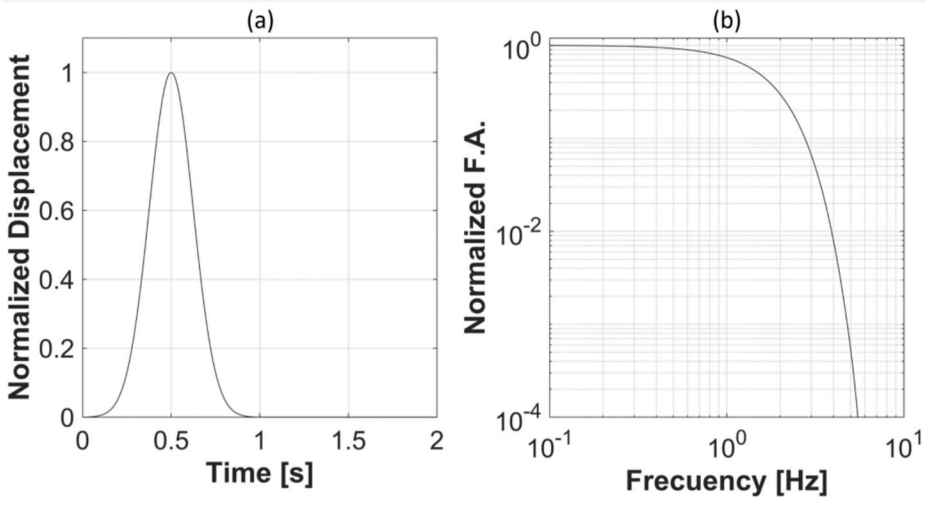


**Fig. 4.** Gabor pulse adopted as source function in the simulations: (a) time-domain pulse and (b) its normalized spectral amplitude.

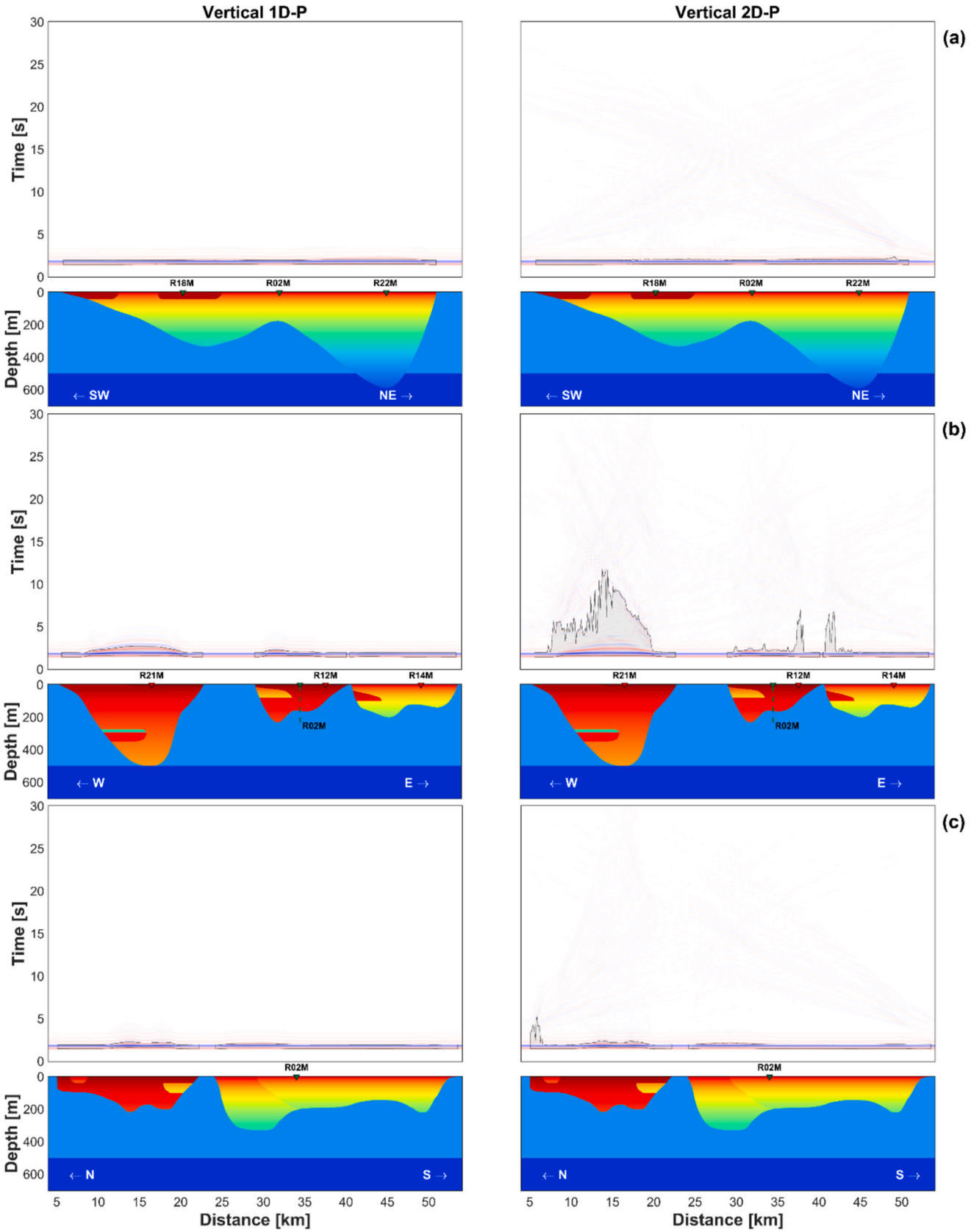


**Fig. 5.** Vertical ground-motion velocities in the (a) CD, (b) EW and (c) NS cross-sections. 1D and 2D stand for one- and two-dimensional incident wavefronts, whereas P stands for P-wave. The shaded areas highlight the time-span between the 5–95% of the Arias Intensity (IA).

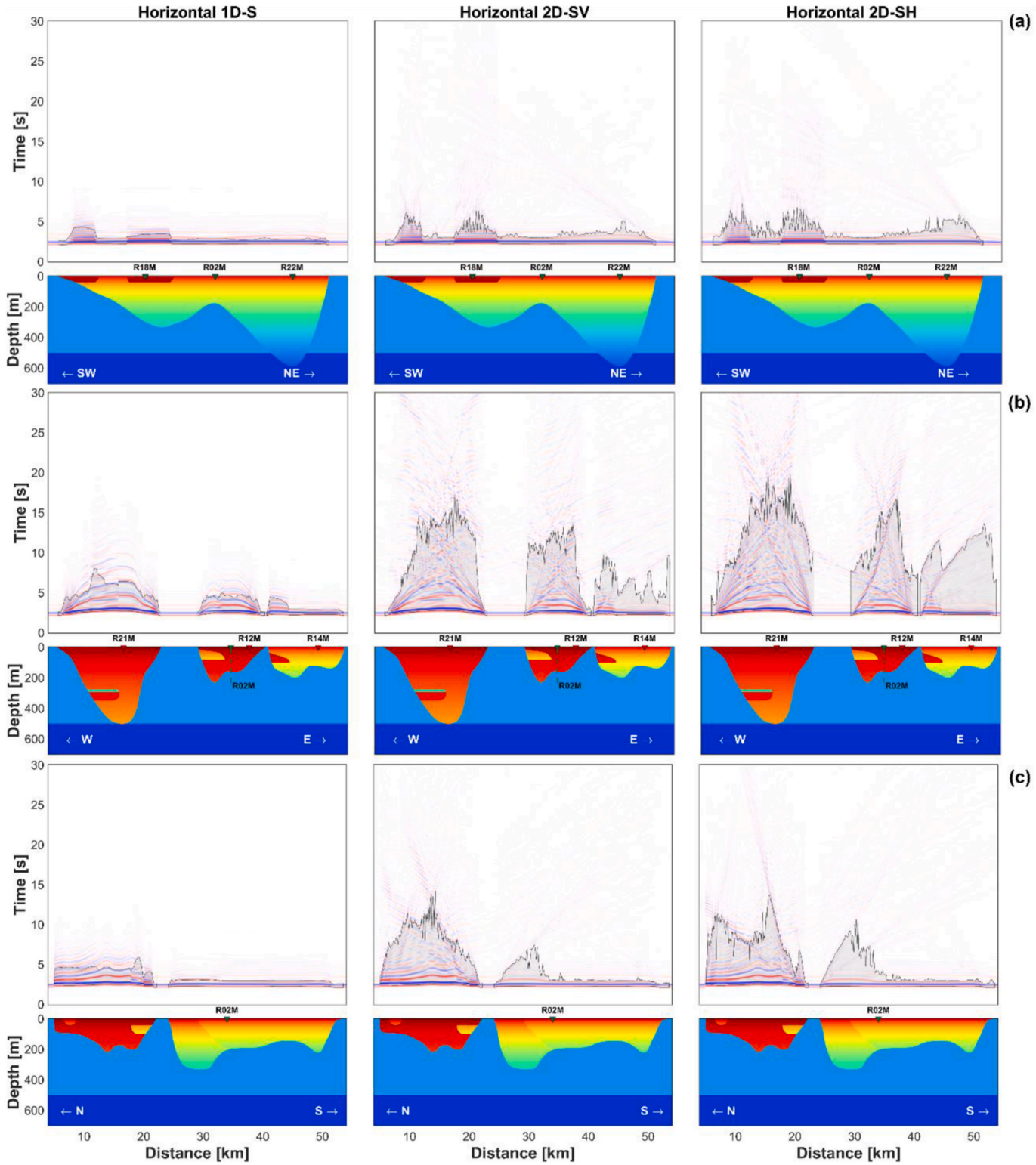


**Fig. 6.** Horizontal ground-motion velocities in the (a) CD, (b) EW and (c) NS cross-sections. 1D and 2D stand for one- and two-dimensional incident wavefronts, whereas S, SV, and SH stand for S-, SV-, and SH-waves. The shaded areas highlight the time-span between the 5–95% of the Arias Intensity (IA).

Santiago Basin. Additionally, they concluded that the location of the rupture nucleation largely influences the observed shaking pattern. Leyton et al. [2] described the surface geology of the Basin and proposed a seismic zonation that considers two areas based on the dynamic properties of the shallower soils, predominant vibration frequencies from HVSR, as well as intensities and damage distribution reported during the 1985 Mw 8.0 Valparaiso Earthquake. According to the study, the geological units IIIa, VI, and VII (Fig. 1), concentrated most of the structural damage observed during the Valparaiso Earthquake (MSK-64 intensities larger than 7.5). Pastén et al. [17] calculated cross-correlations of the vertical component of seismic ambient noise between seismic station pairs to estimate phase velocity dispersion curves between 0.1 and 8.0 Hz. Inversion of the phase-velocity dispersion curves allowed obtaining deep shear wave velocity profiles down to

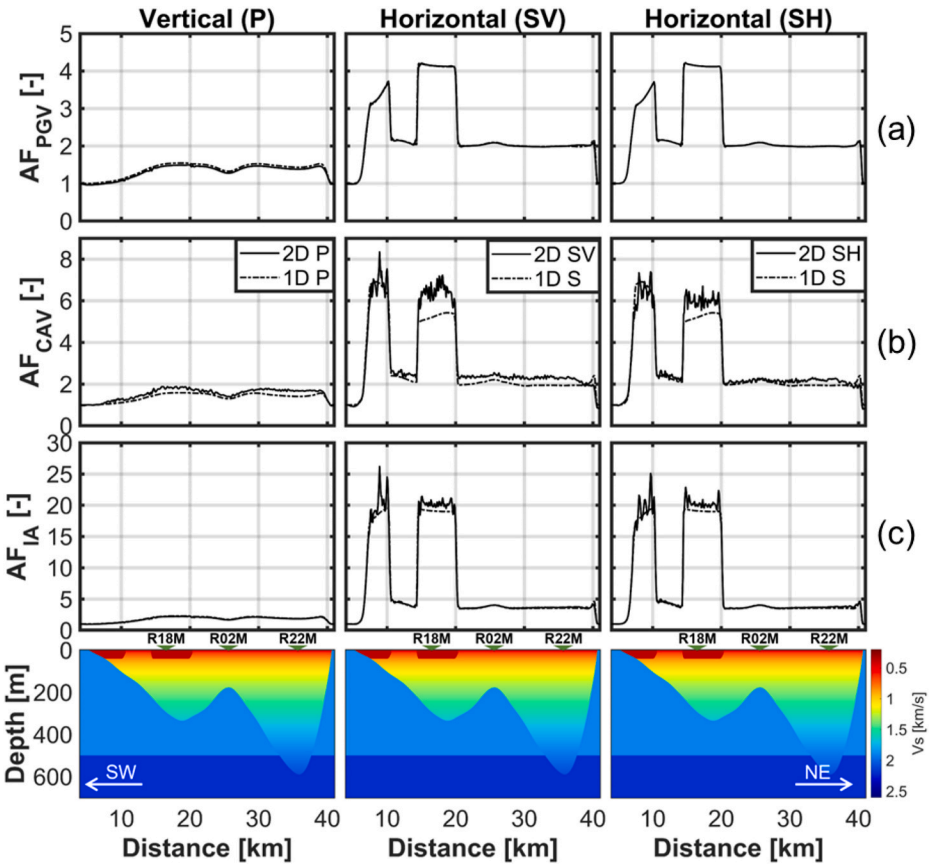


**Fig. 7.** Amplification factors for (a) PGV, (b) CAV, and (c) IA along the CD cross-section in the vertical and horizontal directions.

5 km depth, which were the input of an ambient seismic noise tomography that determined a 3D shear wave velocity model of the Abanico Formation underlying the Santiago city metropolitan area [18]. The resolution of the tomography was unable to define the wave velocities of the shallow soil sediments because of the large interstation distances. The shorter wavelengths detected in the study only allowed defining the Vs profiles at depths larger than 600 m.

The seismic simulations carried out by Pilz et al. [15] presented a series of simplifications: (1) the mesh size that ranges from 60 to 900 m allows propagating waves up to 2.5 Hz, (2) the seismic sources generated complex wave radiation patterns that complicates isolating the contribution of the soil amplification at the surface ground motions, and (3) a single quaternary sediment was considered. To overcome these limitations, our study defines a denser mesh to analyze sites with low Vs values, extending the maximum frequency limit to 5 Hz. Also, vertically-incident plane waves were considered as seismic inputs to simplify the seismic source and facilitate the analysis of site amplification. Finally, our study incorporates different types of soils with various dynamic properties, so it could predict seismic amplifications given the spatial variability of the soils and rock outcrops.

The objectives of this study are (1) to define three representative cross-sections of the soils in the Santiago Basin (EW, NS, and CD cross-sections in Fig. 1), (2) to define the dynamic properties of the different sediments and the bedrock in the cross-sections, based on Vs profiles obtained from geophysical surveys and the seismic noise tomography of Salomón et al. [18], (3) to perform 1D and 2D numerical simulations inducing plane wavefronts from the base of the cross-sections using the finite-difference code 2DFD_DVS [19], (4) to compare the numerical 1D and 2D dynamic responses in the surface of each cross-section, considering the synthetic records, HVSR, as well as amplification and aggravation factors, and (5) to compare the amplification patterns predicted from the 2D models with the seismic records available from the 2015 Mw 8.3 Illapel Megathrust Earthquake.

## 2. Geologic framework

Leyton et al. [2] defined nine soil units in the Basin (Fig. 1) based on the soils of the shallower 30 m and geological maps [20]. They identified that the north of the Basin is filled with silts, clays, sands, and ignimbrite layers. These soft fine-grained soils generate large impedance contrasts with the underlying bedrock (unit VII in Fig. 1). Towards the west, ticker shallow pyroclastic deposits, known as Pudahuel Ignimbrite, can be found in combination with sands, silts, and gravels (unit VI in Fig. 1). These deposits merge with the northern fine-grained soils. The Basin's central part was filled with coarse-grained sediments as a consequence of the coalescence of the Mapocho and Maipo rivers. These materials, known as the Santiago gravels (unit II, Fig. 1), are mainly sandy gravels of medium to high density, with high strength and stiffness. To the east, alluvial deposits are located at the slope toe of the Andes Mountains. These sediments are moderately stiff and mainly composed of blocks and subangular gravels in a sandy-clayey matrix.

## 3. Numerical models

In this study, we analyzed the EW, NS and CD cross-sections along the Santiago Basin shown in Fig. 1. The geological models in the cross-sections were defined from geological logs of water wells with more than 200 m depth obtained from the General Directorate of Water (GDW) and studies from Fernández [21,22], Fock [23], Milovic [24], Rauld [25], Sellés and Gana [26], and Wall et al. [27]. The inferred geological models considered the most dominant soil layers and disregarded inclusions of thin soil layers since the shortest wavelengths analyzed in our study are in the order of 40 m. In cases where the water wells did not reach the bedrock, we assumed that the deepest soil layer in the well

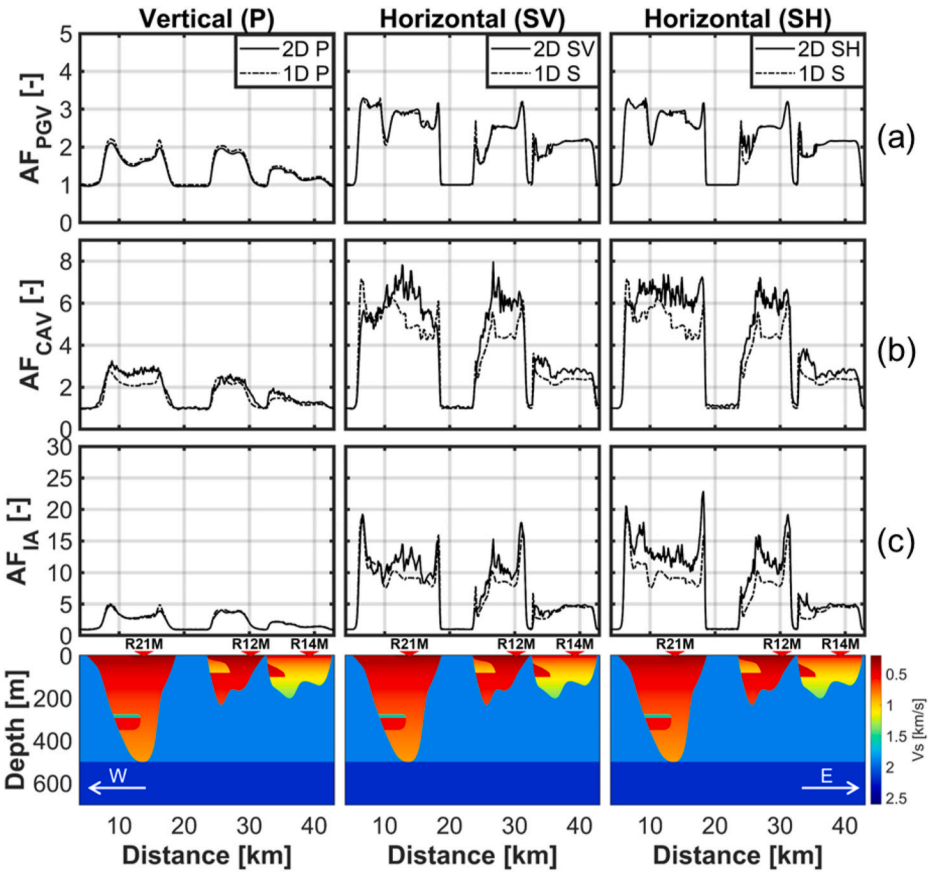


**Fig. 8.** Amplification factors for (a) PGV, (b) CAV, and (c) IA along the EW cross-section in the vertical and horizontal directions.

extended to the interface with the bedrock inferred from the gravimetric studies [3–5]. We also considered the surface geology reported in Leyton et al. [2] for the shallower soil layers. The northern part of the Basin was defined using information from the 2D geological cross-sections proposed by Galvez [28]. The three defined cross-sections are shown in Fig. 2.

### 3.1. Dynamic properties

The Vs of the soils in the cross-sections were calculated from seismic ambient noise records reported by Pastén [12], complemented with additional geophysical surveys in areas with scarce information. The surveys mainly focused in the northwest area of the Basin, to generate a robust model for the fine-grained soils, which are expected to have the largest seismic amplifications. In each study site, we recorded 40-min of seismic ambient noise with four Tromino 3G sensors (triaxial seismographs with a natural frequency of ~4.5 Hz). The adopted sensors array depended on the available space at each site. For instance, the use of rectangular and linear arrays allowed inter-sensor distances between 20 and 200 m. We cross-correlated the vertical records of the sensors following the methodology developed by Pastén et al. [17], based on Ekström et al. [29], to obtain a representative phase velocity dispersion curve. We also calculated single station Rayleigh wave ellipticities with the RayDec software developed by Hobiger et al. [30] and determined predominant frequencies using the HVSR method. We performed a joint inversion in two steps following the methodology developed in Hobiger et al. [31] using the Dinver subroutine of the Geopsy software [32]. The first step of the inversion process adjusted the dispersion curve with velocity profiles searched in a range of Vs and layer thicknesses that depended primarily on the minimum wavelengths obtained from the dispersion curves. The second step consisted of a joint inversion that considered the dispersion curve, the ellipticity curve, and the predominant frequency of the site. The joint inversion narrows the search range of the Vs based on the results obtained in the first step. This methodology allows obtaining deeper Vs profiles that satisfy the target constraints. Fig. 3 shows examples of 10 Vs profiles obtained in fine-grained soils and 14 Vs profiles in gravel.

Based on the geological logs, we defined a transition zone in the NS cross-section (Clayey gravel, clay and gravel, sandy clay, clayey sand in Fig. 2) between the rock outcrop in the center of the profile and the Santiago gravels. The definition of the Vs model in this area relies on few measurements of the average shear wave velocity of the upper 30 m ($Vs_{30}$), which vary between values reported for the northern fine-grained soils and the Santiago gravels.

The variation of Vs with depth for gravels, fine-grained soils, and the transition zone was captured with the model proposed by Pilz et al. [15].

$$V_s = V_{s0} + dV_s \bullet \sqrt{\frac{Z}{1m}} \quad (1)$$

The parameters $Vs_0$ and dVs were adjusted to fit the Vs model to the Vs profiles shown in Fig. 3. For the transition zone, we defined the parameters seeking to obtain shallow Vs values larger than those of the fine-grained soils but lower than those of the gravels, as well as keeping the same Vs rate of increase with depth (dVs) than gravels. The parameters adopted for each soil type in the Basin are shown in Table 1. Fig. 3 shows the models adopted for the fine-grained soils and gravels discretized every 5 m (to be consistent with the grid spacing of the numerical models defined below). The densities of the materials were selected based on the reference values reported by Bonnefoy-Claudet et al. [11].

The Vs of the shallow ignimbrites shown in the CD and EW cross-sections in Fig. 2 was considered constant with a value of 350 m/s

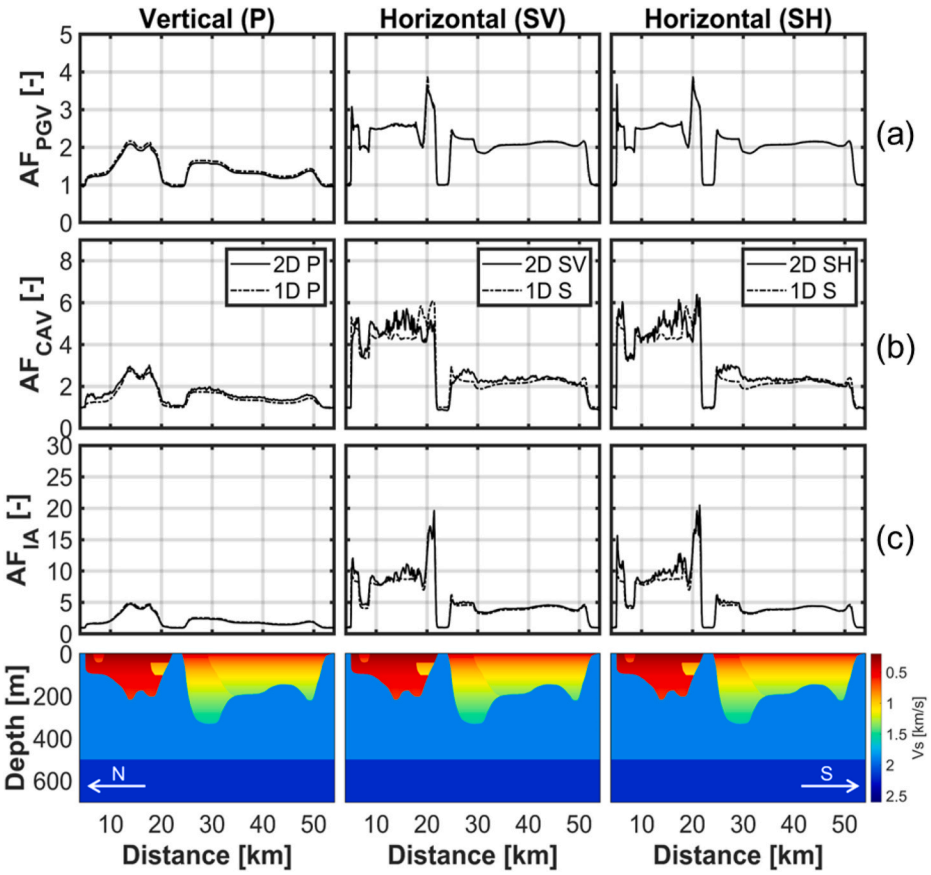


**Fig. 9.** Amplification factors for (a) PGV, (b) CAV, and (c) IA along the NS cross-section in the vertical and horizontal directions.

whereas the deep layer in the EW cross-section was assumed at Vs = 500 m/s, following values reported by Rebolledo et al. [33].

The P-wave velocity (Vp) was estimated according to Kitsunezaki et al. [34], assuming that the soil has a high degree of saturation.

$$V_p = 1.11 \bullet V_s + 1290 \tag{2}$$

This assumption was considered valid for fine-grained soils given the shallow groundwater levels, between 0 and 15 m, reported by Muñoz et al. [44] in the northwest of the Basin. However, this assumption may not be valid in the southeast area where the depths of the groundwater level reach 150 m, causing an overestimation of Vp. Nonetheless, this overestimation in the stiff Santiago's gravel does not affect the relative amplification of the horizontal to the vertical ground-motion components (i.e., HVSR) within the studied frequency range.

The attenuation factors for the S- and P-waves were estimated as [36].

$$Q_s = \frac{V_s}{10} \tag{3}$$

$$Q_p = 2 \bullet Q_s \tag{4}$$

The Vs of the bedrock was estimated from the seismic noise tomography developed by Salomón et al. [18]. The cross-sections discretized the bedrock into 5 layers with Vs gradually varying with the depth from the cross-sections surface (z)

$$V_s = \begin{cases} 1.9\ \text{km/s} & z < 0.5\ km \\ 2.2\ km/s & 0.5\ km \le z < 1\ km \\ 2.8\ km/s & 1\ km \le z < 2\ km \\ 3.1\ km/s & 2\ km \le z < 3\ km \\ 3.4\ km/s & z > 3\ km \end{cases} \tag{5}$$

Fig. 2 shows the Vs models associated with the three geological models of each cross-section.

### 3.2. Numerical simulations

Each cross-section was subjected to three vertically-incident 2D wavefronts: a vertical P-wavefront (2D-P), a horizontal in-plane S-wavefront (2D-SV), and a horizontal out-plane S-wavefront (2D-SH). The surface responses of the 2D simulations were compared with the 1D response of the soil columns at each receiver located at the surface of the model subjected to vertically-incident P- and S-waves (1D-P and 1D-S). In total, five simulations were performed for each cross-section.

Numerical simulations were performed using the finite-difference code 2DFD_DVS [19]. This code allows the propagation of waves in heterogeneous and viscoelastic media in a rectangular domain with a flat free surface condition. The constitutive model of the materials is the generalized Maxwell body. The lateral and bottom boundary conditions are those defined by Emerman and Stephen [37] with maximum attenuation for P- and S-waves.

The depth of the models is 10 km, with a grid spacing Δh = 5 m, which allows simulating response at frequencies up to 5 Hz in areas with the softest soils, considering that the minimum wavelength should be at least 8•Δh. The time step that ensures numerical stability is Δt = $5 \bullet 10^{-4}$ s. The wavefronts are input at 5 km depth in all models and the adopted source function is a Gabor pulse (Equation (6), Fig. 4), with the following parameters: $f_p = \frac{\omega_p}{2\pi} = 0.18\ Hz$, $\gamma = 0.2$, $\theta = 0.0$, and $t_s = 0.45 \bullet \frac{\gamma}{f_p}$.

$$s(t) = e^{-\left[\frac{\omega_p (t - t_s)}{\gamma}\right]^2} \bullet \cos\left[\omega_p (t - t_s) + \theta\right] \tag{6}$$

This pulse has been adopted in similar studies [38,39]. The pulse amplitude decays at about 5 Hz, being consistent with the resolution of

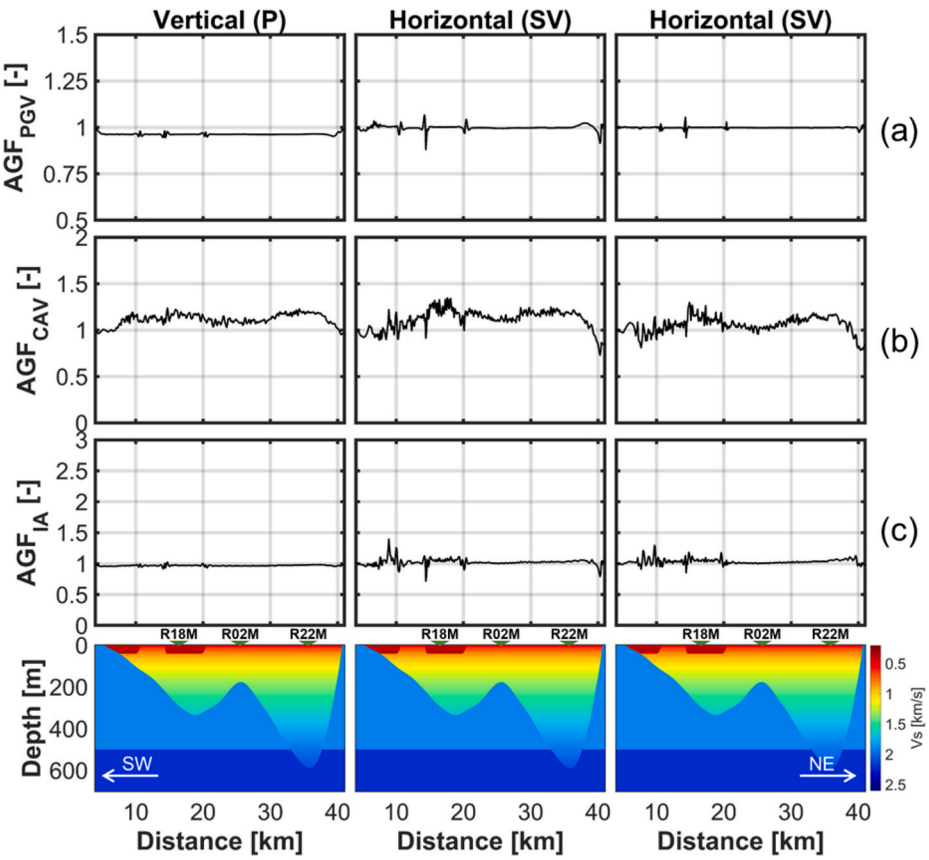


**Fig. 10.** Aggravation factors for (a) PGV, (b) CAV, and (c) IA along the CD cross-section in the vertical and horizontal directions.

the numerical models.

## 4. Numerical results

### 4.1. Surface ground motion

Figs. 5 and 6 show the vertical and horizontal ground-motion velocities at the surface of the three cross-sections subjected to the different analyzed wavefronts: the 1D P-wavefront (1D-P), the 1D S-wavefront (1D-S), the 2D P-wavefront (2D-P), the 2D SV-wavefront (2D-SV), and the 2D SH-wavefront (2D-SH). The figures consider surface receivers every 100 m and the shaded areas in both figures highlight the time-span between the 5–95% of the Arias Intensity (IA).

In the CD cross-section (Figs. 5a and 6a), there are no significant differences between the 1D and 2D results because this cross-section has high stiffness due to the dominant presence of Santiago gravels. However, areas with shallower ignimbrites with low Vs experience larger amplitudes and longer durations of the strong motion in the horizontal direction (Fig. 6a). In the EW cross-section (Figs. 5b and 6b), a considerable increase in the duration of the strong motion can be observed in areas with softer and deeper soil deposits in 2D models. In the east area of the EW cross-section, filled with Santiago gravels, the seismic behaviors of 1D and 2D models are similar to that described for the CD cross-section, except in the horizontal 2D-SH case that is strongly influenced by the surface waves generated on the west boundary. Finally, the NS cross-section (Figs. 5c and 6c) confirms the effects described in the CD and EW cross-sections. The southern area of the NS cross-section, ranging from 23 to 53 km, composed of stiff soils shows slight differences in the horizontal components between the 1D and 2D simulations, except in the transition zone that is influenced by the surface waves generated on the north boundary. On the other hand, the northern area of the cross-section, composed mainly of soft soils, shows longer strong motions in 2D simulations. The prolongation in the duration of the strong motion in this area is not as pronounced as that of the EW cross-section because the deposits are shallower.

### 4.2. Amplification factors

Amplification factors ($AF_{EGMC}$) were calculated to evaluate the surface amplification of various earthquake ground motion characteristics (EGMC) at a soil site ($EGMC_{soil}$) with respect to a reference site ($EGMC_{ref}$).

$$AF_{EGMC} = \frac{EGMC_{soil}}{EGMC_{ref}} \tag{7}$$

A similar amplification analysis was performed by Kristek et al. [39]. The EGMCs selected for this study were the Peak Ground Velocity (PGV), the Peak Ground Acceleration (PGA), the Cumulative Absolute Velocity (CAV, Equation (8)), and the Arias Intensity (IA, Equation (9)).

$$\mathrm{CAV} = \int_0^\infty |a(t)|dt \tag{8}$$

$$IA = \frac{\pi}{2g}\int_0^\infty a(t)^2 dt \tag{9}$$

Here, a(t) is an acceleration time-history and g is the acceleration of gravity.

In this section, the reference site for the evaluation of $AF_{EGMC}$ was a rock outcrop in each cross-section. Figs. 7–9 show $AF_{PGV}$, $AF_{CAV}$, and $AF_{IA}$ along the CD, EW, and NS cross-sections in the vertical and horizontal directions for 1D and 2D analyses. The horizontal $AF_{EGMC}$ are divided into the incident SV- and SH-waves in 2D analyses, and are

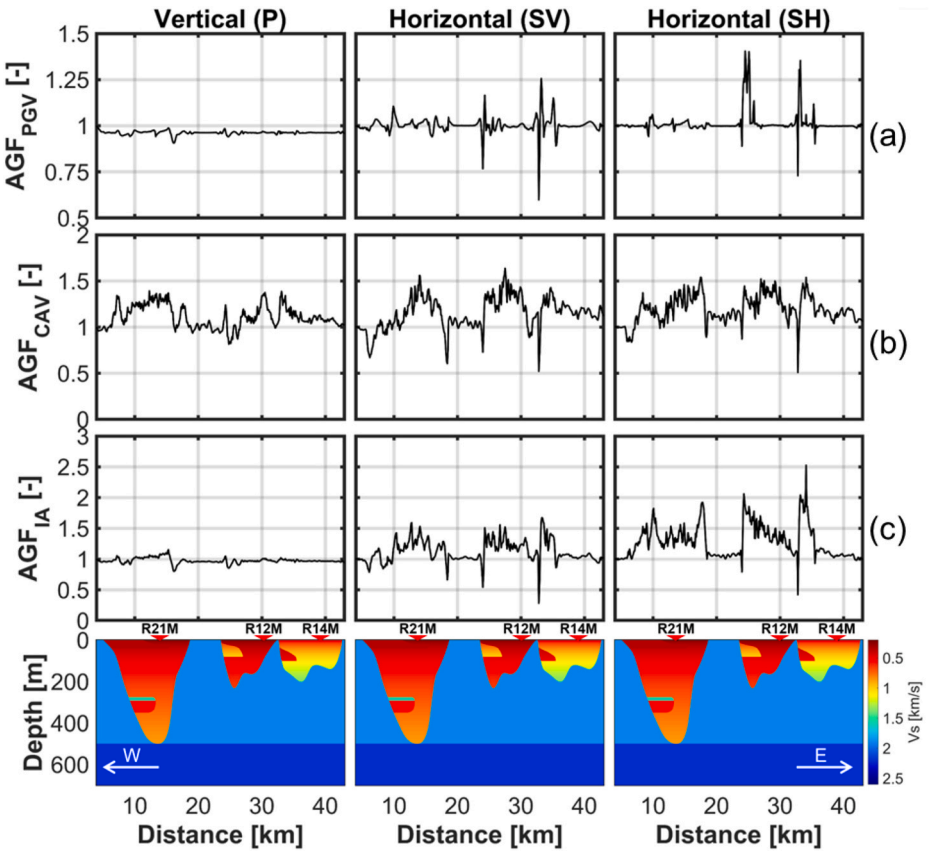


**Fig. 11.** Aggravation factors for (a) PGV, (b) CAV, and (c) IA along the EW cross-section in the vertical and horizontal directions.

compared with the $AF_{EGMC}$ of the incident S-wave in the 1D analyses. The vertical $AF_{EGMC}$ only considers incident P-waves in 1D and 2D analyses.

Vertical $AF_{PGV}$ are mainly lower than 2 in the three cross-sections. The higher vertical $AF_{PGV}$ were found at the boundaries of the soils near the rock outcrops, particularly in soils with lower Vs (central and western areas in the EW cross-section, Fig. 8, and northern area in the NS cross-section, Fig. 9). Horizontal $AF_{PGV}$ (SV and SH) are close to 2 in areas with high Vs, specifically in the northeast and central areas of the CD cross-section and the southern area of the NS cross-section where gravel deposits are found. In contrast, the horizontal $AF_{PGV}$ can reach values up to 4 in areas with lower Vs in the EW and NS cross-sections and on the surface of the ignimbrite deposits in the CD cross-section. Slight differences are evidenced between the $AF_{PGV}$ obtained from 1D and 2D analyses. $AF_{PGA}$ is not shown herein since it resembles closely to $AF_{PGV}$.

$AF_{CAV}$ follow a very similar trend than $AF_{PGV}$ in the stiff soils of the three cross-sections. In contrast, the $AF_{CAV}$ of the softer soils in the cross-sections can reach larger values close to 6. The differences between the $AF_{CAV}$ obtained from 1D and 2D simulations are more pronounced than the differences between the $AF_{PGV}$.

$AF_{IA}$ are considerably larger than the previous AF, reaching a relatively constant value of 4 in the soils with high Vs and maximum values close to 20 on top of the softer sediments. Sharp peaks of $AF_{IA}$ are generated near the contacts of softer soils with rock outcrops. Differences are detected between the $AF_{IA}$ obtained from 1D and 2D simulations, particularly in soft soils.

### 4.3. Aggravation factors

An aggravation factor of an earthquake ground motion characteristic ($AGF_{EGMC}$) at a site of interest was calculated as

$$AGF_{EGMC} = \frac{AF^{2D}_{EGMC}}{AF^{1D}_{EGMC}} \tag{10}$$

Here, $AF^{2D}_{EGMC}$ and $AF^{1D}_{EGMC}$ are the amplification factors of an EGMC at the site of interest calculated from 2D and 1D analyses, respectively. Sites where the $AGF_{EGMC}$ is close to unity show slight differences between the 1D and 2D simulation approaches whereas sites with $AGF_{EGMC}$ >1.25 may be considered as strongly affected by 2D effects [40].

Figs. 10–12 show $AGF_{PGV}$, $AGF_{CAV}$, and $AGF_{IA}$ along the CD, the EW, and the NS cross-sections in the vertical and horizontal directions shown in Figs. 7–9.

Vertical and horizontal $AGF_{PGV}$ and $AGF_{IA}$ in the Santiago gravels in the CD cross-section (Fig. 10) and the southern area of the NS cross-section (Fig. 12) tend to remain close to unity, except in the contacts with the rock outcrops. In contrast, $AGF_{CAV}$ in the gravel tend to exceed unity and tend to show a correlation with the bedrock depth (Fig. 10). An interesting amplification pattern is observed in the east of the EW cross-section (Fig. 11) where a buried pocket of fine-grained soil into gravel causes large $AGF_{EGMC}$, particularly in the horizontal directions. The 1D simulation approach predicts that the fine-grained soil behaves as a damper that reduces the EGMC (Fig. 8), contrary to the 2D simulation prediction.

Vertical $AGF_{PGV}$ and $AGF_{IA}$ in fine-grained soils remain relatively constant close to one. The rest of the AGFs show more pronounced differences in these soils, most likely due to the generation of Rayleigh waves for incident P- and SV-waves, and Love waves for incident SH-waves, causing larger amplifications and longer durations of strong ground motions in 2D simulations.

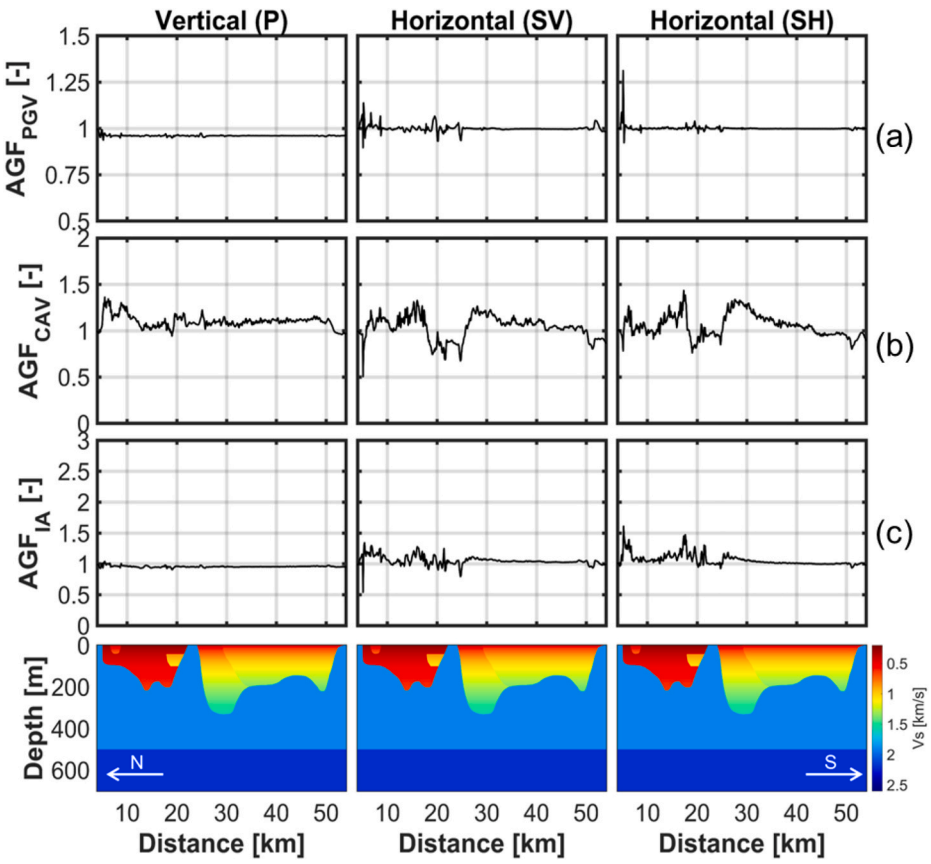


**Fig. 12.** Aggravation factors for (a) PGV, (b) CAV, and (c) IA along the NS cross-section in the vertical and horizontal directions.

## 5. Empirical evidence of seismic amplification

The last large earthquake that affected the urban area of the Santiago City was the 2015 Mw 8.3 Illapel Earthquake. This earthquake occurred at approximately 220 km north of Santiago City and was recorded by several seismic stations installed in the Basin (Fig. 1). To compare the predicted numerical amplification with empirical values, we focused on six seismic stations: R12M, R14M, and R21M installed along the EW cross-section, and R18M, R02M, and R22M installed along the CD cross-section. Stations R12M and R21M are located over the northern fine-grained soils (unit VII, Fig. 1), station R18M is located over an ignimbrite deposit (unit VI, Fig. 1), and stations R02M, R14M, and R22M are located over the Santiago gravels (unit II, Fig. 1). The analyses in this section consider the seismic and synthetic records bandpass filtered between 0.1 Hz and 3.5 Hz.

### 5.1. Amplification factors

To compare seismic records and synthetic ground motions obtained from 2D numerical models, we considered the station R02M as the reference site in the calculation of amplification factors $AF_{EGMC}$ (Equation (7)). $AF_{EGMC}$ were calculated for vertical and horizontal components separately. The horizontal measured seismic records were projected in the longitudinal direction along the cross-sections and compared to the horizontal components obtained from the SV-wave propagation in 2D simulations. The vertical measured seismic records were compared to the vertical components obtained from the P-wave propagation in 2D simulations.

Fig. 13 shows acceleration seismic records and synthetic ground motions at the stations R18M and R02M, from which $AF_{PGA}$ can be determined. In this example, the synthetic $AF_{PGA}$ in the horizontal and vertical directions are lower than the recorded $AF_{PGA}$.

Fig. 14 compares $AF_{EGMC}$ for PGA, PGV, IA, and CAV calculated from the seismic records and the synthetic ground motions in the horizontal and vertical directions. In general, 2D simulations tend to underestimate the amplification factors. This effect is more pronounced in the fine-grained soils in terms of PGA, PGV, and IA. The $AF_{EGMC}$ in sites over gravel (R14M and R22M) remain close to one.

### 5.2. HVSR in seismic stations

We calculated HVSRs using the response of a single surface receiver [41] from 2D and 1D simulations, and compared the results with HVSRs calculated from the seismic records in the six seismic stations shown in Fig. 1.

Synthetic HVSRs were calculated on the surface receivers of each cross-section as the ratio of the smoothed Fourier's spectral amplitudes (sFFT) of the simulated horizontal and vertical ground motions. We selected the receivers closest to the six stations along the EW and CD cross-sections and calculated the HVSR for the following cases:

$$HVSR_{1D} = \frac{sFTT(Horizontal\ 1D - S)}{sFTT(Vertical\ 1D - P)} \tag{11}$$

$$HVSR_{2D} = \frac{sFTT(Horizontal\ 2D - SV)}{sFTT(Vertical\ 2D - P)} \tag{12}$$

The synthetic vertical and horizontal ground motions in Equations (11) and (12) are those shown in Figs. 5 and 6. Fig. 15 compares synthetic and empirical HVSR calculated from the seismic records. Synthetic $HVSR_{1D}$ and $HVSR_{2D}$ fit well the empirical HVSRs in the analyzed frequency band. Synthetic and empirical HVSR amplitudes barely exceed 2 at stations R02M, R14M, and R22M over the Santiago gravels. Synthetic HVSR in the stations R12M, R18M, and R21M capture relatively well the amplitudes and frequencies of the peaks observed in the

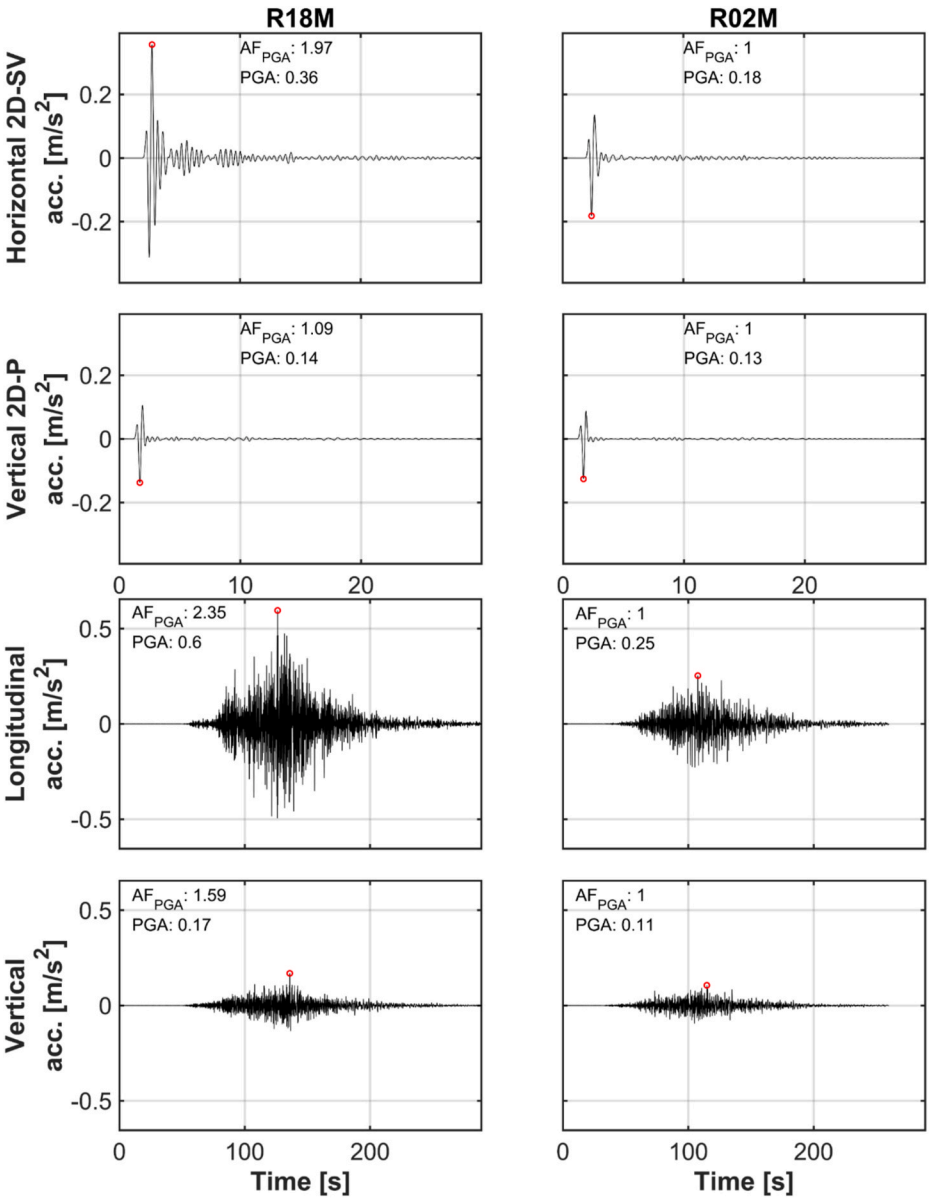


**Fig. 13.** Seismic records obtained at stations R18M and R02M for the 2015 Mw 8.3 Illapel Earthquake compared to synthetic ground motions.

empirical HVSRs.

### 5.3. HVSR in the EW cross-section

Fig. 16 shows the predominant frequencies ($F_0$) and the corresponding peak amplitudes of the $HVSR_{1D}$ and $HVSR_{2D}$ calculated with Equations (11) and (12), respectively, at the surface of the EW cross-section. For every analyzed frequency at a surface receiver, the aggravation factor between $HVSR_{1D}$ and $HVSR_{2D}$ is calculated using Equation (10). These synthetic HVSRs are compared to empirical HVSRs calculated from seismic ambient noise measurements. The bounded areas in grey show the amplitudes larger than 90% the peak $HVSR_{1D}$ amplitude.

Stiff soils show amplitudes generally closer to 2 with the absence of a clear peak amplitude. In contrast, softer soils have considerably higher amplitudes, and their predominant frequencies are inversely correlated with the depth of the bedrock. There are slight differences in the predominant frequencies obtained from 1D and 2D simulations, but large differences in the HVSR amplitudes at frequencies higher than the $F_0$ in areas with soft sediments. In general, synthetic $HVSR_{1D}$ and $HVSR_{2D}$ capture the predominant frequencies obtained from measured HVSR.

The HVSRs and aggravation factors at the surface of the CD and NS cross-sections are shown in Figures A1 and A2 in the Supplementary Material.

### 5.4. SSR in the EW cross-section

Fig. 17 shows the standard spectral ratios calculated for the horizontal components of the 1D and 2D models with Equations (13) and (14), respectively, at the surface of EW cross-section. We considered as a reference the 1D-S response of a site located 3 km away from the edge of the basin (Ref_Horizontal 1D-S). The 1D-S response of this site lacks reflected, refracted, and surface waves generated in 2D models. The bounded areas in the Figure show the amplitudes larger than 90% the peak $HVSR_{1D}$ amplitude (similar to Fig. 16).

$$SSRH_{1D} = \frac{sFFT(Horizontal\ 1D-S)}{sFFT(Ref\_Horizontal\ 1D-S)} \tag{13}$$

$$SSRH_{2D} = \frac{sFFT(Horizontal\ 2D-SV)}{sFFT(Ref\_Horizontal\ 1D-S)} \tag{14}$$

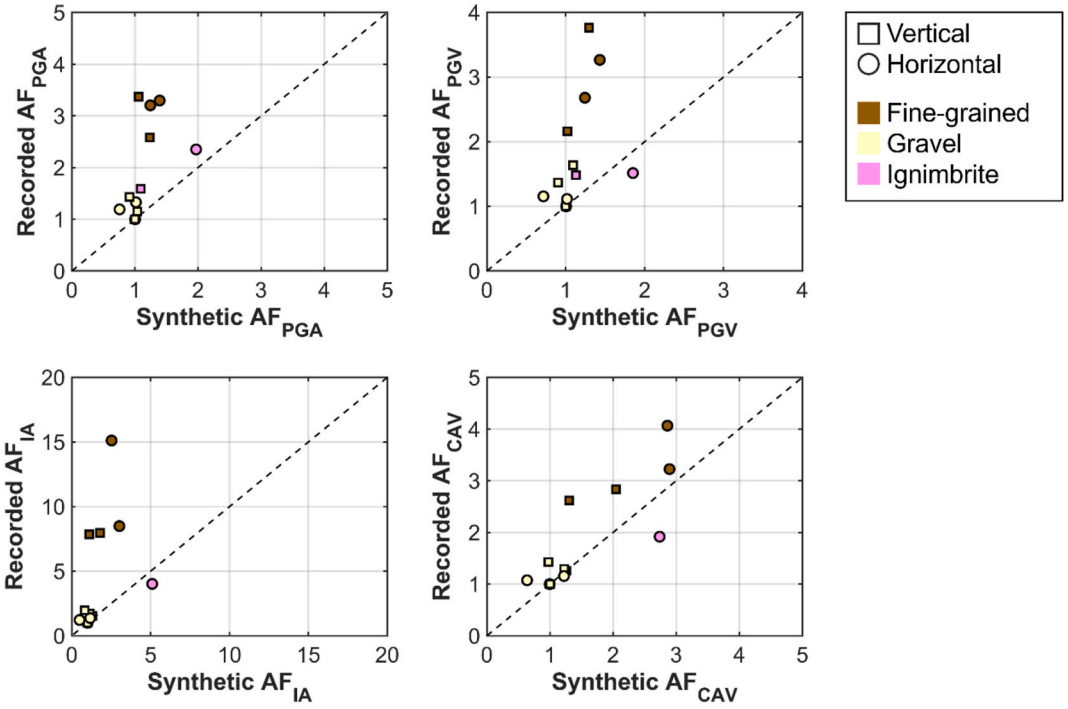


**Fig. 14.** Synthetic and recorded amplification factors (AF) for PGA, PGV, IA, and CAV.

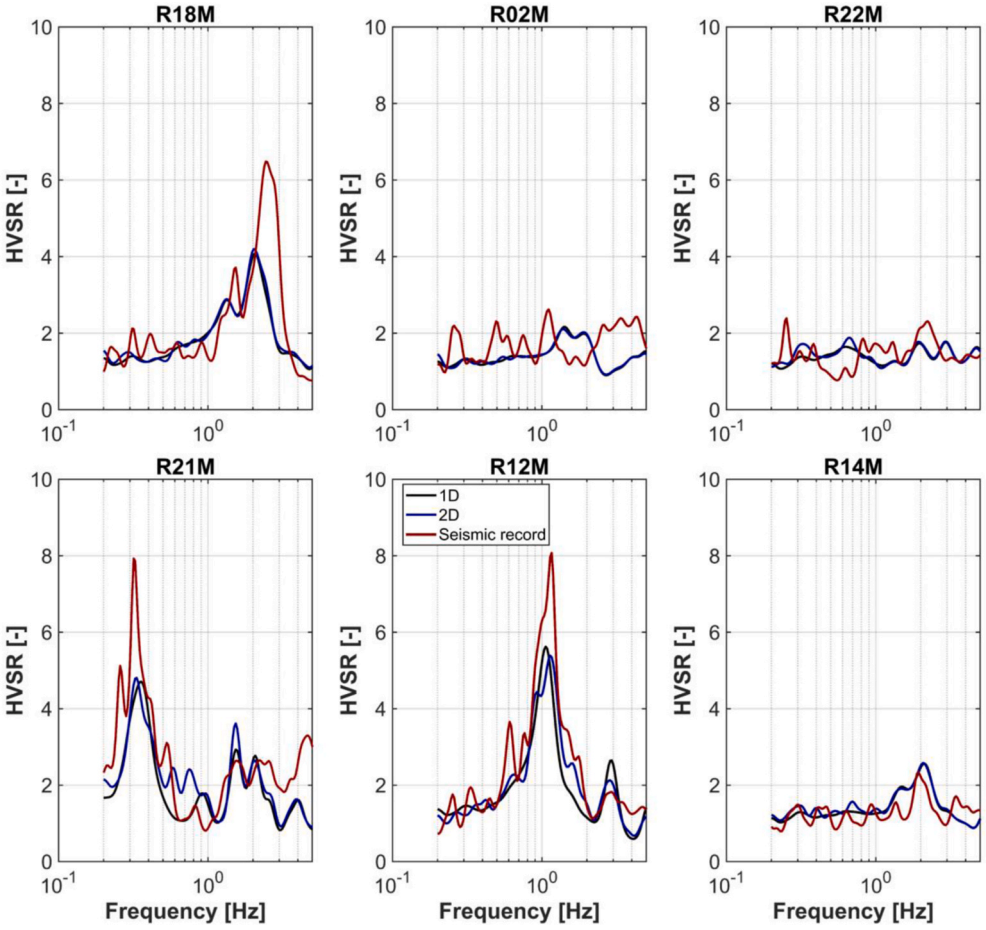


**Fig. 15.** HVSRs calculated from synthetic records (1D, 2D, 2D-SV, and 2D-P) and seismic records at each analyzed seismic station.

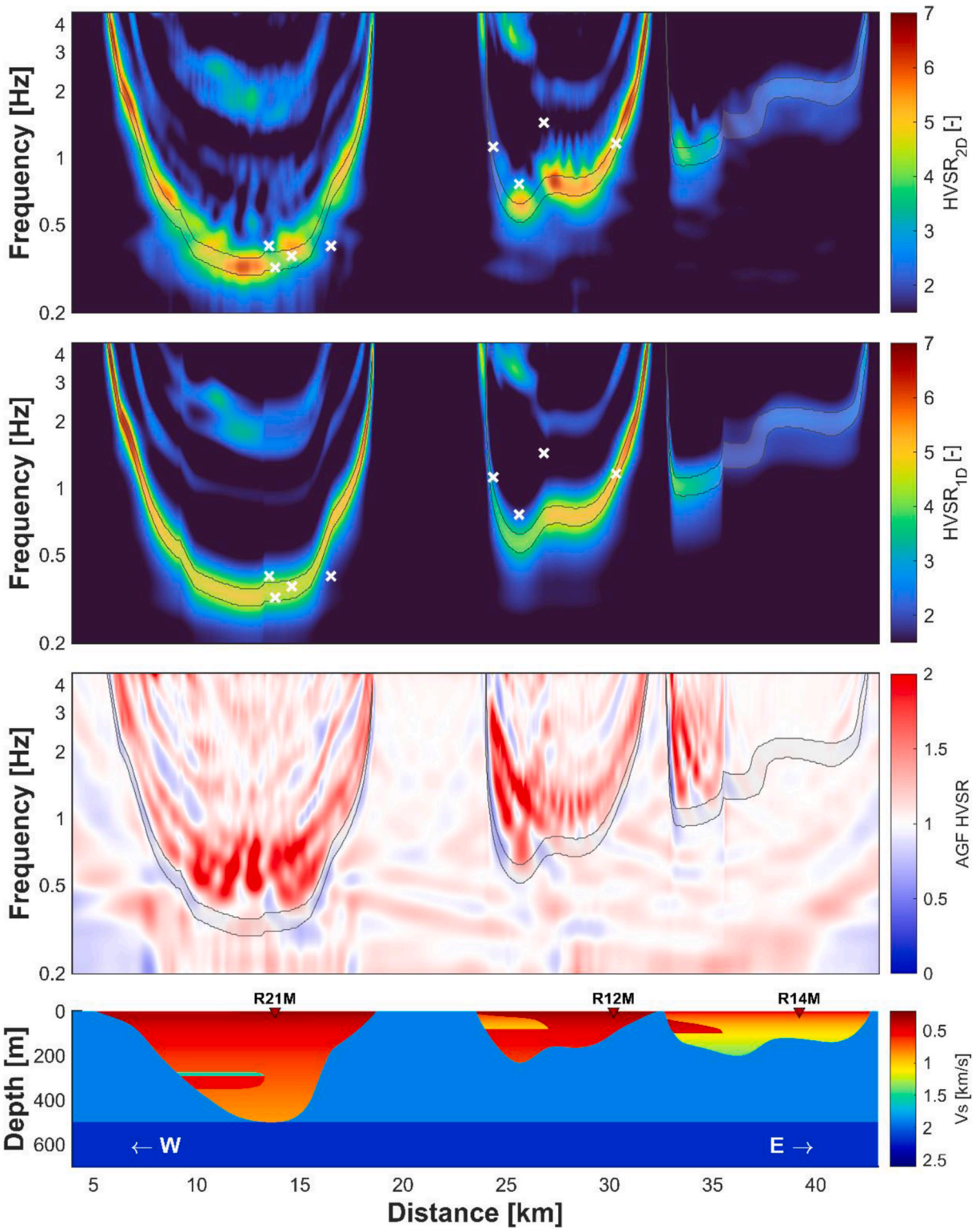


**Fig. 16.** Top panels show the $HVSR_{2D}$ and $HVSR_{1D}$ at the surface of the EW cross-section, compared with measured HVSRs (white crosses). Middle panel shows the AGF of HVSR. The bounded areas in grey show the amplitudes larger than 90% the peak $HVSR_{1D}$ amplitude.

Fig. 17 shows that the estimated predominant frequencies with $SSRH_{1D}$ and $SSRH_{2D}$ are almost identical to those obtained with $HVSR_{1D}$ and $HVSR_{2D}$. In addition, the aggravation factors for HVSR and SSRH are similar, highlighting that the basin effects calculated with 2D simulations are more pronounced for frequencies larger than $F_0$.

The SSRHs and aggravation factors at the surface of the CD and NS cross-sections are shown in Figures A3 and A4 in the Supplementary Material.

## 6. Discussion

The numerical aggravation factors show that 2D amplification patterns do not differ from those predicted by 1D simulations in the Santiago gravels. The reduced difference may be associated with the low

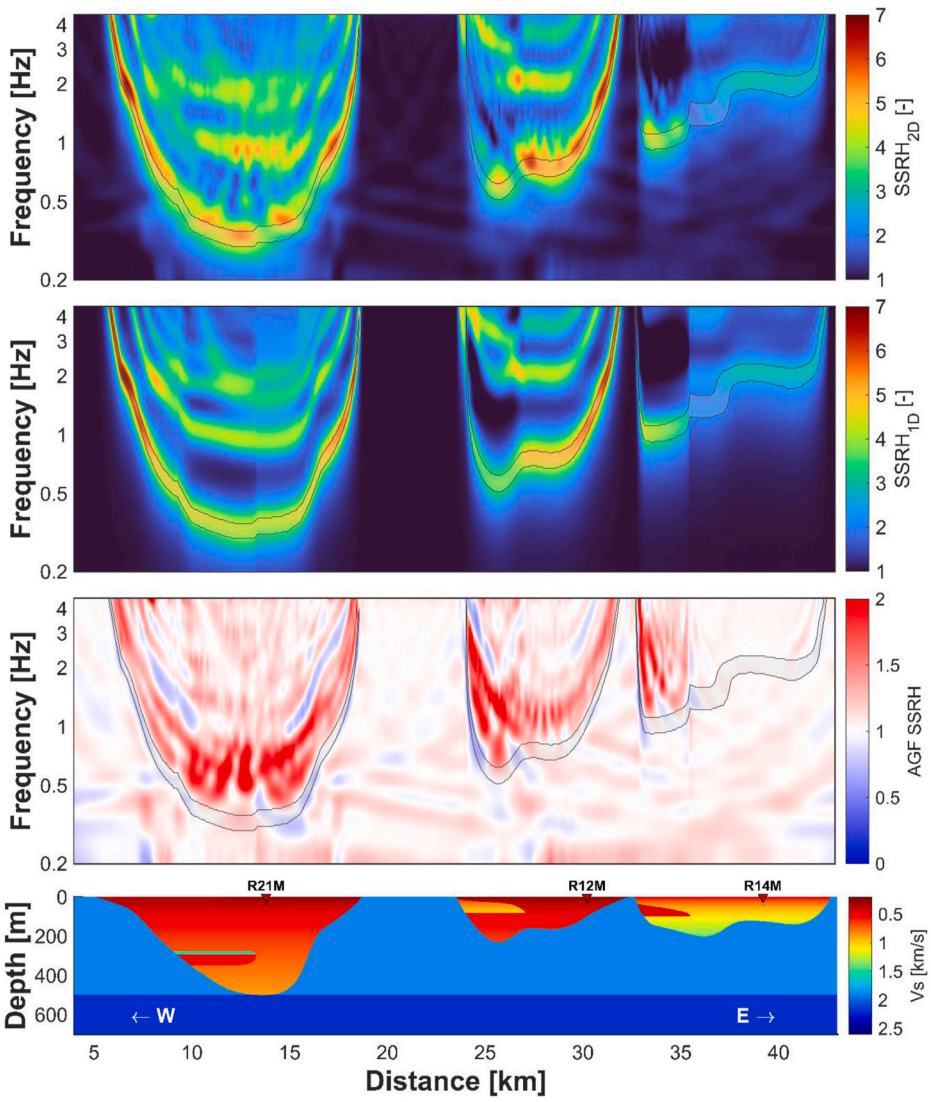


**Fig. 17.** Top panels show the $SSRH_{2D}$ and $SSRH_{1D}$ at the surface of the EW cross-section. Middle panel shows the AGF of SSRH. The bounded areas in grey show the amplitudes larger than 90% the peak $HVSR_{1D}$ amplitude.

impedance contrast between the soil and the underlying bedrock, which hinders 2D effects generated by the bedrock geometry.

On the other hand, 2D effects are more evident in softer sediments and even more pronounced as the depths of the deposits increase. The surface response of 2D simulations have considerably longer durations than those obtained in 1D simulations (evidenced by larger $AGF_{CAV}$ in Fig. 11). This is mainly due to the generation of surface waves in 2D simulations in addition to the refraction and reflection of body waves.

Areas with strong spatial variations of Vs show the largest aggravation factors, which is probably related to the geometric stiffening provided by the strong lateral contrasts in the dynamic properties of the materials considered in 2D models. In these areas, we also noticed differences in HVSR amplitudes, but slight variations in the predicted predominant frequencies (Fig. 16). Moreover, AGFs sharply vary as approaching areas with shallow softer soils overlying the bedrock or stiffer gravels (see Fig. 11), in agreement with results from Zhu et al. [42].

The differences between the synthetic responses obtained from 2D simulations and the recorded from the 2015 Illapel Earthquake (Fig. 13) in stations over fine-grained soils (R12M and R21M) with respect to stations over Santiago gravels (R02M, R14M, and R22M) are also due to the differences in the seismic sources. The Illapel Earthquake was a thrust earthquake with a long epicentral distance of 220 km (Fig. 1), which favored attenuation of high-frequency waves. The remaining low-frequency waves could cause larger amplification in deposits with low predominant frequencies, such as those where stations R12M and R21M are installed. In contrast, the synthetic seismic waves in our models were generated by a pulse at 5 km depth, which was not affected by geometric attenuation. To improve the comparison between synthetic and recorded responses, a larger number of seismic events and scatter of the input motions with longer durations and several energy pulses of different frequency content should be considered [40].

Another important source of differences is the material damping, which is partly accounted in our models by the wave quality factors, Qs and Qp. For simplicity, these material parameters were linked to the wave velocities in our study (Equations (3) and (4)). However, their values should be carefully defined if more realistic predictions are expected for the seismic response of the Santiago Basin.

The Vs model introduced in this study in combination with the input wavefronts reproduce HVSR similar to those calculated from earthquake and seismic ambient noise records in the northern fine-grained soils and the Santiago gravels. In the case of fine-grained soil, the predominant frequencies are strongly related to the depth of the soil-bedrock interface due to the high impedance contrast. Moreover, the gradient-like velocity

model of the Santiago gravels combined with a soil thickness in the order of hundreds of meters favor the largest soil Vs values are reached near the bedrock (1.9 km/s). Hence, the impedance contrast of the soil layers as well as that of the soil layers and the bedrock remain reduced. The low impedance contrast tends to generate flatter SSRH and HVSR, which can be seen in areas with deeper deposits of Santiago gravels in the CD cross-section and in the HVSRs of the stations R02M and R22M (Fig. 15). The predominant frequencies in the ignimbrites are underestimated indicating that either the actual Vs is higher than the assumed value or the deposit thickness is lower than that adopted. More measurements are required in areas with lower information density, such as the ignimbrite deposits and the transition zone defined in the NS cross-section.

Considering an inclined incident wavefront would boost the high frequency of the synthetic ground motion across de sections [43]. The extent of this effect depends mainly on the incidence angle and the geometry of the soil bedrock interface. This effect would be much larger in softer soils.

## 7. Conclusions

The numerical simulations show that the Santiago Basin develops 2D seismic amplification in areas dominated by fine-grained soils with low Vs. These effects are linked to refracted and reflected waves, in addition to the generation of surface waves, that can only be captured by 2D simulations. In contrast to 1D simulations, 2D simulations predict a prolongation of the duration of the strong motion, that becomes more pronounced in deeper deposits.

In contrast, seismic amplification of stiff soils with higher Vs can be reasonably captured by both 1D and 2D simulations, which means that the stiff soils in the Santiago Basin do not suffer from 2D effects.

The numerical results presented in this study are consistent with empirical evidence gathered from the 2015 Mw 8.3 Illapel Earthquake records along the CD and EW cross-sections. Similar amplification factors are obtained for gravels and ignimbrites and more pronounced empirical amplification in fine-grained soils, which may be related to the long-period surface waves generated by the earthquake. In the frequency domain, synthetic HVSRs are in good agreement with empirical HVSRs obtained from earthquake and seismic ambient noise records. The peak frequencies and amplitudes from the synthetic HVSRs agree with the empirical values over fine-grained soils whereas the flat HVSRs over gravels are similar to empirical observations. Synthetic HVSRs are similar to synthetic SSRHs and both show larger aggravation factors at frequencies larger than the predominant frequency.

## Author statement

J. Bustos co-developed the cross-sections, run the numerical simulations, and lead the writing of the paper.

C. Pastén lead the research project and supervised the work from the MSc students involved in the paper (J. Bustos, D. Pavez, and M. Acevedo).

D. Pavez co-developed the geological cross-sections and tested their numerical responses.

M. Acevedo defined the shear-wave velocity models used in the cross-sections.

S. Ruiz contributed with the research methodology, the paper writing, and the result analysis.

R. Astroza contributed with the research methodology, the paper writing, and the result analysis.

## Declaration of competing interest

The authors declare that they have no known competing financial interests or personal relationships that could have appeared to influence the work reported in this paper.

## Data availability

Data will be made available on request.

## Acknowledgements

Support for this research was provided by the ANID FONDECYT Grant N°1190995 and the National Laboratory for High Performance Computing (NLHPC) of the University of Chile.

## Appendix A. Supplementary data

Supplementary data to this article can be found online at https://doi.org/10.1016/j.soildyn.2022.107569.

## References

[1] Ruiz S, Madariaga R. Historical and recent large megathrust earthquakes in Chile. Tectonophysics 2018;733:37–56. https://doi.org/10.1016/j.tecto.2018.01.015.
[2] Leyton F, Sepulveda SA, Astroza M, Rebolledo S, Acevedo P, Ruiz S, et al. Seismic zonation of the Santiago Basin, Chile. 5th Int. Conf. Earthq. Geotech. Eng 2011: 1–11. Paper No. SMSLF.
[3] Araneda M, Avendaño M, Merlo C. Modelo gravimétrico de la Cuenca de Santiago, etapa III final. In: IX congreso geológico chileno; 2000. p. 404–8.
[4] González FA, Maksymowicz A, Díaz D, Villegas L, Leiva M, Blanco B, et al. Characterization of the depocenters and the basement structure, below the central Chile Andean Forearc: a 3D geophysical modelling in Santiago Basin area. Basin Res 2018;30:799–815. https://doi.org/10.1111/bre.12281.
[5] Yañez G, Muñoz M, Flores-Aqueveque V, Bosch A. Gravity derived depth to basement in Santiago Basin, Chile: implications for its geological evolution, hydrogeology, low enthalpy geothermal, soil characterization and geo-hazards. Andean Geol 2015;42:147–72.
[6] Fernández J, Pastén C, Ruiz S, Leyton F. Damage assessment of the 2015 Mw 8.3 Illapel earthquake in the north-Central Chile. Nat Hazards 2019;96:269–83. https://doi.org/10.1007/s11069-018-3541-3.
[7] Ruiz S, Klein E, del Campo F, Rivera E, Poli P, Metois M, et al. The seismic sequence of the 16 september 2015 $M_w$ 8.3 Illapel, Chile, earthquake. Seismol Res Lett 2016; 87:789–99. https://doi.org/10.1785/0220150281.
[8] Astroza M, Ruiz S, Astroza R. Damage assessment and seismic intensity analysis of the 2010 (Mw 8.8) Maule Earthquake. Earthq Spectra 2012;28:145–64. https://doi.org/10.1193/1.4000027.
[9] Astroza M, Monge J. Seismic microzones in the city of Santiago. Relation damage-geological unit. In: Fourth international conference on seismic zonation. Stanford, CA, USA; 1991. p. 595–601.
[10] Vergara L, Verdugo R. Condiciones geológicas-geotécnicas de la cuenca de Santiago y su relación con la distribución de daños del terremoto del 27F. Obras y Proy 2015:52–9. https://doi.org/10.4067/s0718-28132015000100007.
[11] Bonnefoy-Claudet S, Baize S, Bonilla LF, Berge-Thierry C, Pasten C, Campos J, et al. Site effect evaluation in the basin of Santiago de Chile using ambient noise measurements. Geophys J Int 2009;176:925–37. https://doi.org/10.1111/j.1365-246X.2008.04020.x.
[12] Pasten C. Respuesta sísmica de la Cuenca de Santiago. Tesis para optar al grado de Magister en Ingeniería Geotécnica. Universidad de Chile; 2007.
[13] Molnar S, Cassidy JF, Castellaro S, Cornou C, Crow H, Hunter JA, et al. Application of microtremor horizontal-to-vertical spectral ratio (MHVSR) analysis for site characterization: state of the art. Surv Geophys 2018;39:613–31. https://doi.org/10.1007/s10712-018-9464-4.
[14] Nakamura Y. A method for dynamic characteristics estimation of subsurface using microtremor on the ground surface. Q. Reports Railw. Tech. Res. Inst. 1989;30: 25–33.
[15] Pilz M, Parolai S, Stupazzini M, Paolucci R, Zschau J. Modelling basin effects on earthquake ground motion in the Santiago de Chile basin by a spectral element code. Geophys J Int 2011;187:929–45. https://doi.org/10.1111/j.1365-246X.2011.05183.x.
[16] Pilz M, Parolai S, Picozzi M, Wang R, Leyton F, Campos J, et al. Shear wave velocity model of the Santiago de Chile basin derived from ambient noise measurements: a comparison of proxies for seismic site conditions and amplification. Geophys J Int 2010;182:355–67. https://doi.org/10.1111/j.1365-246X.2010.04613.x.
[17] Pastén C, Sáez M, Ruiz S, Leyton F, Salomón J, Poli P. Deep characterization of the Santiago Basin using HVSR and cross-correlation of ambient seismic noise. Eng Geol 2016;201:57–66. https://doi.org/10.1016/j.enggeo.2015.12.021.
[18] Salomón J, Pasten C, Ruiz S, Leyton F, Saez M, Rauld R. Shear wave velocity model of the Abanico Formation underlying the Santiago City Metropolitan Area, Chile, using ambient seismic noise tomography. Geophys J Int 2021;225:1222–35.
[19] Moczo P, Kristek J, Galis M, Pazak P, Balazovjech M. The finite-difference and finite-element modeling of seismic wave propagation and earthquake motion. Acta Phys Slovaca 2007;57:177–406. https://doi.org/10.2478/v10155-010-0084-x.
[20] Valenzuela G. Suelo de fundación del gran Santiago. Boletín 33. Instituto de Investigaciones Geológicas (Chile); 1978.

[21] Fernández JC. Respuesta sísmica de la cuenca de Santiago, Región Metropolitana de Santiago. Carta Geológica de Chile, Serie Geología Ambiental. Servicio Nacional de Geología y Minería; 2003.
[22] Fernández JC. Estudio geológico-ambiental para la planificación territorial del sector Tiltil. Universidad de Chile; 2001.
[23] Fock A. Cronología y tectónica de la exhumación en el Neógeno de los Andes de Chile central entre los 33° y los 34°S. Universidad de Chile; 2005.
[24] Milovic J. Estudio geológico-ambiental para el ordenamiento territorial de la mitad sur de la cuenca de Santiago. Universidad de Concepción; 2000.
[25] Rauld R. Análisis morfoestructural del frente cordillerano Santiago Oriente, entre el Río Mapocho y quebrada de Macul. Universidad de Chile; 2002.
[26] Sellés D, Gana P. Geología del área Talagante-San Francisco de Mostazal. Región Metropolitana de Santiago y del Libertador General Bernardo O'Higgins. Servicio Nacional de Geología y Minería.; 2001.
[27] Wall R, Sellés D, Gana P. Área Tiltil-Santiago, Región metropolitana. Mapas Geológicos. 11. Servicio Nacional de Geología y Minería; 1999.
[28] Galvez C. Microzonificación sísmica de los sectores de Lampa y Batuco, Región Metropolitana, Chile. Universidad de Chile; 2012.
[29] Ekström G, Abers Ga, Webb SC. Determination of surface-wave phase velocities across USArray from noise and Aki's spectral formulation. Geophys Res Lett 2009; 36:5–9. https://doi.org/10.1029/2009GL039131.
[30] Hobiger M, Bard PY, Cornou C, Le Bihan N. Single station determination of Rayleigh wave ellipticity by using the random decrement technique (RayDec). Geophys Res Lett 2009;36:1–5. https://doi.org/10.1029/2009GL038863.
[31] Hobiger M, Cornou C, Wathelet M, Di Giulio G, Knapmeyer-Endrun B, Renalier F, et al. Ground structure imaging by inversions of Rayleigh wave ellipticity: sensitivity analysis and application to European strong-motion sites. Geophys J Int 2013;192:207–29. https://doi.org/10.1093/gji/ggs005.
[32] Wathelet M. Geopsy geophysical signal database for noise array processing. Software. Grenoble: LGIT; 2005.
[33] Rebolledo S, Lagos J, Verdugo R, Lara M. Geological and geotechnical characteristics of the Pudahuel ignimbrite , Santiago , Chile. Geol. Soc. London IAEG 2006:1–10.
[34] Kitsunezaki C, Goto N, Kobayashi Y, Ikawa T, Horike M, Saito T, Kurota T, Yamane K, Okuzumi K. Estimation of P- and S- wave velocities in deep soil deposits for evaluating ground vibrations in earthquake. J. Japan Soc. Nat. Disaster Sci. 1990;9:1–17.
[36] Makra K, Chávez-García FJ. Site effects in 3D basin using 1D and 2D models: an evaluation of the differences based on simulations of the seismic response of Euroseistest. Bulletin of Earthquake Engineering 2016;14:1177–94. https://doi.org/10.1007/s10518-015-9862-7.
[37] Emerman SH, Stephen RA. Comment on "Absorbing boundary conditions for acoustic and elastic wave equations" by R. Clayton and B. Engquist. Bull Seismol Soc Am 1983;73:661–5.
[38] Chávez-García FJ. Site effects in Parkway Basin: comparison between observations and 3-D modelling. Geophys J Int 2003;154(3):633–46. https://doi.org/10.1046/j.1365-246X.2003.02055.x.
[39] Kristek J, Moczo P, Bard P-Y, Hollender F, Stripajová S. Computation of amplification factor of earthquake ground motion for a local sedimentary structure. Bull Earthq Eng 2018. https://doi.org/10.1007/s10518-018-0358-0.
[40] Moczo P, Kristek J, Bard P-Y, Stripajová S, Hollender F, Chovanová Z, et al. Key structural parameters affecting earthquake ground motion in 2D and 3D sedimentary structures. Bull Earthq Eng 2018. https://doi.org/10.1007/s10518-018-0345-5.
[41] Lermo J, Chávez-García FJ. Site effect evaluation using spectral ratios with only one sation. Bull Seismol Soc Am 1993;83:1574–94. https://doi.org/10.1002/bate.200690188.
[42] Zhu C, Chávez-García FJ, Thambiratnam D, Gallage C. Quantifying the edge-induced seismic aggravation in shallow basins relative to the 1D SH modelling. Soil Dynam Earthq Eng 2018;115:402–12. https://doi.org/10.1016/j.soildyn.2018.08.025.
[43] Oral E, Ayoubi P, Ampuero JP, Asimaki D, Bonilla LF. Kathmandu Basin as a local modulator of seismic waves: 2-D modelling of non-linear site response under obliquely incident waves. Geophys J Int 2022;231(3):1996–2008.
[44] Muñoz M, Garat P, Flores-Aqueveque V, Vargas G, Rebolledo S, Sepúlveda SA, et al. Estimating low-enthalpy geothermal energy potential for district heating in Santiago basineChile (33.5 °S). Renew Energy 2015;76:186–95. https://doi.org/10.1016/j.renene.2014.11.019.